

Slope-Guided Mamba and Angular-Refined Transformer for Light Field Super-Resolution

Li Jin, Jian Huang, Junde Lu, Shuai Wang, Hao Sheng, Jie Wu*
Hangzhou International Innovation Institute, Beihang University, Hangzhou, China
{ljin01, hj, ljd2406107, shuaiwang, shenghao, jiewu}@buaa.edu.cn

Abstract—Light Field Super-Resolution (LFSR) necessitates accurate modeling of spatial-angular correlations while preserving intrinsic 4D ray coherence. However, maintaining such high-dimensional consistency remains challenging, primarily due to two inherent limitations in prevailing modeling paradigms. First, spatial and angular dimensions are often modeled in a decoupled manner, restricting early cross-dimensional interaction and leading to geometric inconsistencies. Moreover, although continuous sequence modeling paradigms show promise in representing epipolar structures, their rigid scanning mechanisms fundamentally conflict with epipolar geometry, limiting geometry-aware feature aggregation. To address these challenges, we propose a hybrid light field super-resolution network, termed SMART, which integrates a Slope-Guided Mamba and an Angular-Refined Transformer to effectively overcome these limitations. Specifically, we introduce an angular-modulated spatial module to bridge the decoupling gap, incorporating angular priors to strengthen spatial-angular correlation modeling. To mitigate the scan-geometry mismatch, we propose a manifold-aligned trajectory module that enables geometry-consistent sequence modeling along epipolar structures. Experiments on five benchmarks demonstrate that SMART achieves state-of-the-art performance, surpassing previous methods by 0.42 dB (PSNR) with significantly reduced artifacts.

Index Terms—Light Field Super-Resolution, State Space Models, Transformer, Epipolar Plane Image

I. INTRODUCTION

Light field imaging records the spatial-angular distribution of light rays, enabling sophisticated applications such as depth estimation and 3D reconstruction [1], [2]. However, hardware-constrained trade-offs between spatial resolution and angular density typically result in low-resolution sub-aperture images (SAIs), which significantly limit downstream performance. Consequently, Light Field Super-Resolution (LFSR) has emerged as a pivotal technique to restore high-frequency details while preserving 4D epipolar geometry, thereby overcoming hardware bottlenecks and enabling high-quality applications such as virtual reality and autonomous driving. Despite its promise, LFSR is hindered by insufficient spatial-angular modeling, particularly in occluded regions [3].

To address this core issue, early CNN-based methods (e.g., DistgSSR [4]) employed specific convolution kernels to de-

couple the 4D light field subspaces. However, due to local receptive fields, they struggle to capture long-range cross-view dependencies. Subsequent transformer-based architectures typically adopt a decoupled processing paradigm for spatial and angular information. For instance, EPIT [2] employs serial spatial convolution and angular transformers, while LFT [5] utilizes recurrent spatial and angular transformer modules for feature interaction. Although these methods mitigate the deficiencies in long-range context modeling, they primarily rely on shallow feature concatenation mechanisms when integrating the decoupled branches. Consequently, this decoupling paradigm lacks deep geometric awareness and spatial-angular synergy, limiting the ability to achieve global consistency and accurate reconstruction of high-frequency details.

Furthermore, within the realm of LFSR, deep spatial-angular consistency is directly manifested as distinct linear structures in Epipolar Plane Images (EPIs). Leveraging the long-range linearity of EPIs, State Space Models (SSMs) [6] offer an efficient sequence modeling framework with linear complexity. However, existing state-of-the-art architectures based on SSMs [7], [8] have failed to surmount this geometric representation hurdle. As shown in Fig. 1(a), scene information in the EPI domain manifests as continuous slanted trajectories governed by disparity, rather than being distributed across a regular orthogonal grid. Regrettably, most current SSM-based LFSR methods directly inherit the rigid grid-based scanning patterns from Visual Mamba [6], resulting in a fundamental scanning-geometry mismatch. Specifically, whether referring to MLFSR [7], which introduces bidirectional scanning to capture long-range dependencies, or LFMamba [8], which employs channel-wise lightweight SSMs to facilitate feature fusion, these approaches artificially fragment the physical manifold of EPIs. This isolation of correlated pixels during serialization dilutes information and scatters attention, hindering focus on geometrically consistent epipolar lines and constraining feature extraction precision.

To bridge these gaps, we propose SMART (Slope-Guided Mamba and Angular-Refined Transformer). This hybrid architecture unifies geometry-aligned sequence modeling with structure-aware optimization, synergizing transformer’s texture extraction with mamba’s geometric consistency.

Specifically, to rectify the insufficient spatial-angular synergy inherent in existing decoupled methods, we propose the Angular-Modulated Spatial module (AMS). While leveraging Query-Key based attention to capture intra-view spatial

This work was partially supported by the Advanced Materials-National Science and Technology Major Project(No.2024ZD0607800), the National Natural Science Foundation of China (No.62372023), the Zhejiang Provincial Natural Science Foundation of China (Nos.LQN25F020028, LMS25F020006, LZ24F030012) and the Research Start-up Funds of Hangzhou International Innovation Institute of Beihang University (Nos.2024KQ087, 2024KQ012).

*Corresponding author.

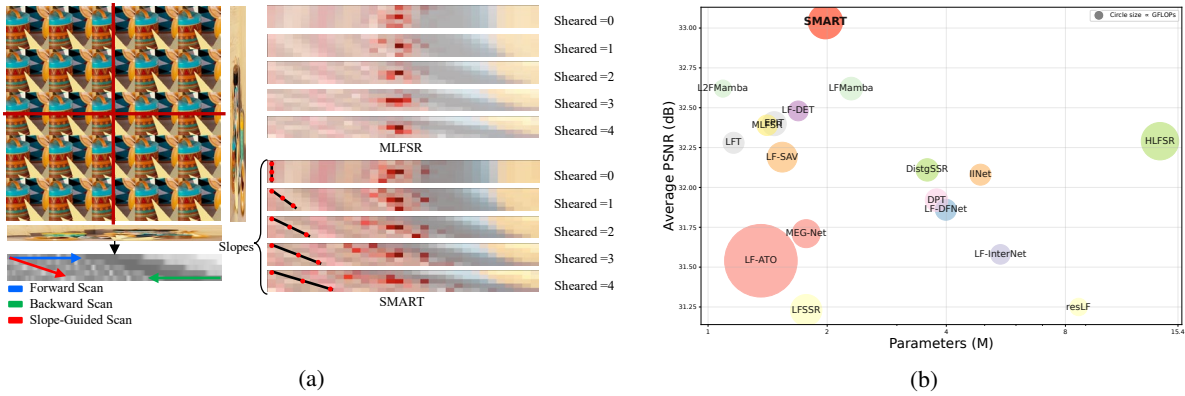


Fig. 1. Visual analysis and performance comparison. (a) Left: Illustration of the geometric-structural mismatch between the EPI structure and the traditional mamba scanning pattern. Right: Heatmaps comparing traditional mamba and SMART at the same spatial location across different sheared EPIs. (b) Comparison of accuracy and model scales between SMART and state-of-the-art methods.

context, this module injects angular priors derived from the macro-pixel layout into the attention maps as structural biases. By incorporating these angular constraints, the model effectively reconstructs high-frequency details in occluded regions, ensuring comprehensive feature completion and geometric consistency. Simultaneously, we propose the Manifold-Aligned Trajectory module (MAT), which innovatively employs a slope-guided geometric scanning strategy to address the scan-geometry mismatch. Capitalizing on the unique EPI structure, we explicitly estimate the local slope k governed by disparity and utilize it as a baseline for sampling offsets. This allows the scanning path to adaptively warp, breaking rigid grid constraints to ensure state transitions occur strictly along geometrically consistent epipolar lines rather than irrelevant background pixels. As illustrated in Fig. 1(a), this mechanism aggregates features from the same spatial point across views along their precise geometric trajectories. Experiments on five standard datasets validate the effectiveness of our approach. As shown in Fig. 1(b), SMART achieves a new SOTA of 33.04 dB / 0.9478 with efficient parameters and GFLOPs, surpassing L²Fmamba [9] by 0.42 dB. Qualitative results in Fig. 3 confirm that SMART restores sharp text outlines and intricate textures while effectively suppressing distortion artifacts. The contributions can be summarized as follows:

(1) We propose SMART, a hybrid network that synergizes the content refinement capabilities of transformers with the geometric consistency modeling of mamba to preserve 4D light field coherence. (2) We design a slope-guided adaptive scanning mechanism that utilizes estimated EPI slopes k to break rigid grid constraints, enabling mamba to aggregate features along geometrically consistent trajectories. (3) Extensive evaluations on five benchmark datasets demonstrate that SMART achieves new SOTA results in PSNR and SSIM, significantly outperforming existing methods.

II. METHODS

A. Methodology Overview

Problem Formulation. The light field feature is generally represented as a 4D tensor $L \in \mathbb{R}^{U \times V \times H \times W}$, where (U, V)

and (H, W) denote the angular and spatial resolutions, respectively. The goal of LFSR is to reconstruct a high-resolution light field $L_{HR} \in \mathbb{R}^{U \times V \times \alpha H \times \alpha W}$ from its low-resolution counterpart $L_{LR} \in \mathbb{R}^{U \times V \times H \times W}$, where α represents the upscaling factor. This problem defines a mapping function \mathcal{F} :

$$L_{SR} = \mathcal{F}(L_{LR}; \Theta), \quad (1)$$

where L_{SR} denotes the reconstructed LF and Θ represents the learnable parameters of the network.

SMART Architecture. To address this problem, we propose SMART, a cascaded network for LFSR. As shown in Fig. 2, the pipeline comprises three stages: feature extraction, deep structure interaction, and reconstruction.

$$F_0 = H_{Sf}(L_{LR}), \quad (2)$$

$$F_i = AMS_i(MAT_i(F_{i-1})), \quad i = 1, \dots, N, \quad (3)$$

$$L_{HR} = H_{Rec}(F_N), \quad (4)$$

where H_{Sf} extracts shallow features from the input L_{LR} using convolution layers. The interaction stage employs MAT module to reinforce epipolar consistency using EPI features, followed by AMS module for disparity and texture encoding. Finally, H_{Rec} upsample F_N via sub-pixel convolution to recover the high-resolution L_{HR} .

B. Manifold-Aligned Trajectory Module

Applying SSMs [6] to LFSR faces a mismatch between fixed scanning trajectories and the underlying epipolar geometry of the light field. Specifically, scene points in EPIs manifest as slanted lines rather than orthogonal grid patterns. Consequently, standard raster scans compel SSMs to model spatially adjacent but geometrically unrelated pixels, disrupting the inherent manifold continuity. To address this, we propose the MAT module. It shifts sequence modeling from blind spatial scanning to geometry-aware manifold traversal, guiding feature extraction along continuous epipolar structures.

To leverage the inherent manifold structure, we reorganize F_{i-1} into a horizontal EPI stack $X_{EPI}^{(H)} \in \mathbb{R}^{(U \cdot H) \times W \times V \times C}$, mapping scene depth to linear slopes in the V - W plane. We define a disparity hypothesis set $\mathcal{K} = \{k_1, \dots, k_M\}$. For each

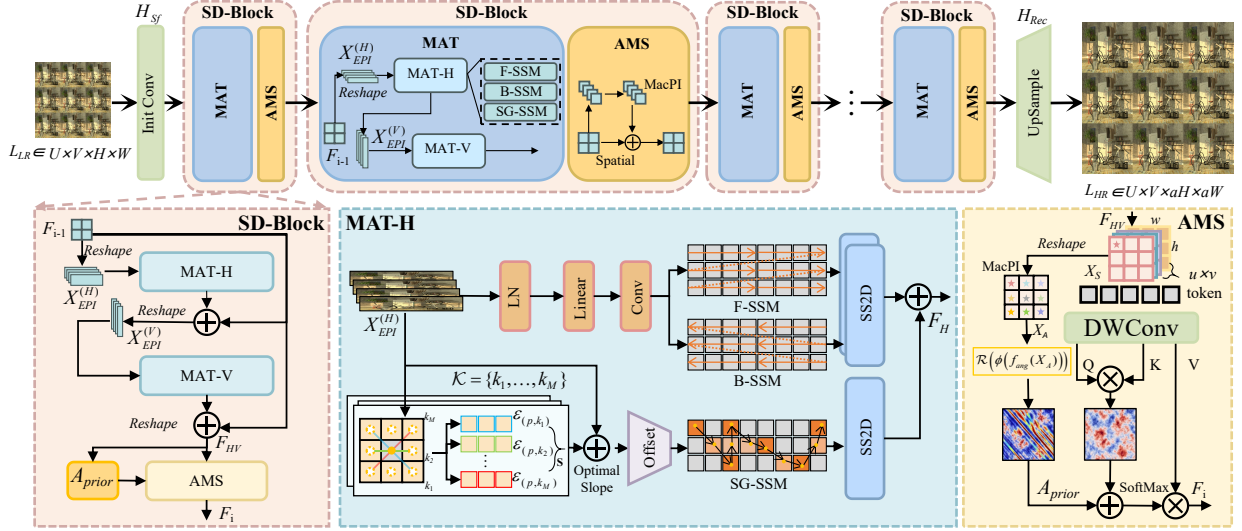


Fig. 2. The overview of the SMART. The interaction stage consists of N cascaded Structure-Detail blocks (SD-Blocks), where each block comprises a MAT module and an AMS module. The MAT module includes horizontal (H) and vertical (V) EPI processing units, which share a structurally identical design.

pixel p , we sample features along the trajectory corresponding to k_m within an angular neighborhood Ω . We quantify the degree of consistency among pixels along the trajectory by computing the consistency cost \mathcal{E} :

$$\mathcal{E}(p, k_m) = \frac{1}{C} \sum_{c=1}^C \text{Var} \left(X_{EPI}^{(H)}(p + \delta \cdot \vec{v}_{k_m}) \mid \delta \in \Omega \right), \quad (5)$$

where \vec{v}_{k_m} is the direction vector defined by k_m , and $\text{Var}(\cdot)$ computes the trajectory variance. p represents the currently processed pixel point, C denotes the number of feature channels, and δ is the offset within the angular neighborhood Ω used for sampling. Lower \mathcal{E} indicates minimal feature dispersion, corresponding to the true scene geometry.

We convert the cost \mathcal{E} into a probability distribution P via Softmax and derive the optimal slope \mathbf{S} as the expectation:

$$P(p, k_m) = \frac{\exp(-\lambda \mathcal{E}(p, k_m))}{\sum_{j=1}^M \exp(-\lambda \mathcal{E}(p, k_j))}, \quad (6)$$

$$\mathbf{S}(p) = \sum_{m=1}^M k_m \cdot P(p, k_m), \quad (7)$$

where λ is a learnable parameter, $\mathbf{S} \in \mathbb{R}^{U \times V \times H \times W}$ encodes dominant EPI directions and provides a continuous and differentiable geometric manifold constraint for feature scanning.

Leveraging the geometric prior \mathbf{S} , our slope-guided adaptive scanning mechanism to align SSM receptive fields with the manifold. The input $X_{EPI}^{(H)}$ are flattened into three parallel sequences: forward X_{fwd} , backward X_{bwd} , and the slope-guided path X_{sg} . While the raster paths capture bidirectional context, X_{sg} transcends grid limits, utilizing geometric priors to dynamically reconstruct the scanning trajectory.

The slope prior \mathbf{S} generates coordinate offsets and sorting indices, allowing the SSM to transcend grid limits. This facilitates scanning along epipolar lines, aggregating long-range in-

formation from geometrically correlated regions. Specifically, \mathbf{S} is embedded via an MLP and concatenated with feature F . This combined input drives an offset network to produce spatial offsets $\Delta P \in \mathbb{R}^{2 \times H \times W}$ and temporal sorting indices $\mathcal{I} \in \mathbb{R}^{1 \times H \times W}$. $[\cdot; \cdot]$ denotes channel-wise concatenation.

$$(\Delta P, \mathcal{I}) = \Psi([\text{MLP}(\mathbf{S}); F_{i-1}]), \quad (8)$$

where Ψ denotes the offset and index generation network. We resample the original features F_{i-1} using ΔP to achieve feature aggregation along the slope direction, yielding the aligned features F_{align} . Subsequently, F_{align} is reordered based on \mathcal{I} to establish the slope-guided dynamic scanning trajectory.

These sequences are processed by a shared selective scan kernel, fused via summation, refined by an MLP, and reshaped, incorporating a residual connection to get the output F_H :

$$F_H = \text{MLP} \left(\sum_{d \in \{fwd, bwd, sg\}} \text{SSM}(X_d) \right) + F_{i-1}, \quad (9)$$

where X_d denotes the input sequences. fwd , bwd , and sg denote the forward, backward, and slope-guided scanning orders, respectively. Analogously, for the vertical EPI stack, we transform the features F_H into $X_{EPI}^{(V)}$ to obtain the corresponding output F_V . The final output of the MAT is the fused representation F_{HV} , which combines both F_H and F_V .

This design aligns feature extraction with light transport geometry, facilitating consistent high-frequency reconstruction.

C. Angular-Modulated Spatial Module

Existing LFSR methods typically decouple spatial and angular processing, fusing them only at the final stage. This separation ignores the 4D coherence, leading to artifacts caused by geometric inconsistency. To address this, we introduce the AMS module, which intertwines spatial with angular geometry by leveraging angular correlations as attention biases.

TABLE I

QUANTITATIVE COMPARISON (PSNR / SSIM) OF DIFFERENT STATE-OF-THE-ART LIGHT FIELD IMAGE SR METHODS FOR X4 UPSCALING FACTOR. THE LAST COLUMN SHOWS THE AVERAGE RESULTS. **BOLD** INDICATES THE BEST PERFORMANCE, AND UNDERLINED INDICATES THE SECOND BEST RESULTS.

Methods	#Params.	EPFL	HCInew	HCIold	INRIA	STFgantry	Average
Bilinear	–	24.567 / 0.8158	27.085 / 0.8397	31.688 / 0.9256	26.226 / 0.8757	25.203 / 0.8261	26.95 / 0.8566
Bicubic	–	25.264 / 0.8324	27.715 / 0.8517	32.576 / 0.9344	26.952 / 0.8867	26.087 / 0.8452	27.72 / 0.8701
VDSR [10]	0.67M	27.246 / 0.8777	29.308 / 0.8823	34.810 / 0.9515	29.186 / 0.9204	28.506 / 0.9009	29.81 / 0.9066
EDSR [11]	38.89M	27.833 / 0.8854	29.591 / 0.8869	35.176 / 0.9536	29.656 / 0.9257	28.703 / 0.9072	30.19 / 0.9118
RCAN [12]	15.36M	27.907 / 0.8863	29.694 / 0.8886	35.359 / 0.9548	29.805 / 0.9276	29.021 / 0.9131	30.36 / 0.9141
resLF [13]	8.65M	28.260 / 0.9035	30.723 / 0.9107	36.705 / 0.9682	30.338 / 0.9412	30.191 / 0.9372	31.24 / 0.9322
LFSSR [14]	1.77M	28.596 / 0.9118	30.928 / 0.9145	36.907 / 0.9696	30.585 / 0.9467	30.570 / 0.9426	31.52 / 0.9370
LF-ATO [15]	1.36M	28.514 / 0.9115	30.880 / 0.9135	36.999 / 0.9699	30.711 / 0.9484	30.607 / 0.9430	31.54 / 0.9373
LF-InterNet [16]	5.48M	28.812 / 0.9162	30.961 / 0.9161	37.150 / 0.9716	30.777 / 0.9491	30.365 / 0.9409	31.61 / 0.9388
LF-DFnet [17]	3.99M	28.774 / 0.9165	31.234 / 0.9196	37.321 / 0.9718	30.826 / 0.9503	31.147 / 0.9494	31.86 / 0.9415
MEG-Net [18]	1.78M	28.749 / 0.9160	31.103 / 0.9177	37.287 / 0.9716	30.674 / 0.9490	30.771 / 0.9453	31.72 / 0.9399
LF-IINet [19]	4.89M	29.038 / 0.9188	31.331 / 0.9208	37.620 / 0.9734	31.034 / 0.9515	31.261 / 0.9502	32.06 / 0.9429
DistgSSR [4]	3.58M	28.992 / 0.9195	31.380 / 0.9217	37.563 / 0.9732	30.994 / 0.9519	31.649 / 0.9535	32.12 / 0.9440
LFSSR-SAV [20]	1.54M	29.368 / 0.9223	31.450 / 0.9217	37.497 / 0.9721	31.270 / 0.9531	31.362 / 0.9505	32.19 / 0.9439
HLFSR-SSR [21]	13.87M	29.196 / 0.9222	31.571 / 0.9238	37.776 / 0.9742	31.241 / 0.9534	31.641 / 0.9537	32.28 / 0.9455
DPT [1]	3.79M	28.939 / 0.9170	31.196 / 0.9188	37.412 / 0.9721	30.964 / 0.9503	31.150 / 0.9488	31.93 / 0.9414
LFT [5]	1.16M	29.255 / 0.9210	31.462 / 0.9218	37.630 / 0.9735	31.205 / 0.9524	31.860 / 0.9548	32.28 / 0.9447
EPIT [2]	1.47M	29.339 / 0.9197	31.511 / 0.9231	37.677 / 0.9737	31.372 / 0.9526	32.179 / 0.9571	32.42 / 0.9452
LF-DET [22]	1.66M	29.473 / 0.9230	31.558 / 0.9235	37.843 / 0.9744	31.389 / 0.9534	32.139 / 0.9573	32.48 / 0.9463
MLFSR [7]	1.41M	29.283 / 0.9218	31.562 / 0.9235	37.828 / 0.9745	31.241 / 0.9531	32.029 / 0.9567	32.389 / 0.9459
LFmamba [8]	2.30M	<u>29.840</u> / 0.9256	<u>31.695</u> / 0.9249	<u>37.912</u> / 0.9748	<u>31.808</u> / 0.9551	31.846 / 0.9533	32.621 / 0.9467
L ² Fmamba [9]	1.09M	29.681 / 0.9233	31.674 / 0.9243	37.864 / 0.9745	31.728 / 0.9543	<u>32.198</u> / 0.9574	<u>32.623</u> / 0.9468
Ours	1.98M	30.284 / <u>0.9243</u>	31.761 / 0.9259	38.128 / 0.9749	32.458 / <u>0.9540</u>	32.572 / 0.9597	33.040 / 0.9478

TABLE II

ABLATION STUDY ON THE EFFECTIVENESS OF THE PROPOSED COMPONENTS.

AMS	A_{prior}	MAT	EPFL	HCInew	HCIold	INRIA	STFgantry	Average
			24.567/0.8158	27.085/0.8397	31.688/0.9256	26.226/0.8757	25.203/0.8261	26.954/0.8566
✓			27.996/0.8897	29.835/0.8892	35.448/0.9552	29.929/0.9293	29.401/0.9160	30.522/0.9159
	✓		29.491/0.9144	31.216/0.9194	37.495/0.9718	31.846/0.9491	31.580/0.9520	32.326/0.9414
		✓	29.661/0.9161	31.271/0.9203	37.426/0.9716	31.939/0.9498	31.375/0.9508	32.335/0.9417
✓	✓		29.537/0.9203	31.496/0.9214	37.777/0.9743	31.674/0.9534	32.053/0.9559	32.507/0.9451
✓	✓	✓	30.284/0.9243	31.761/0.9259	38.128/0.9749	32.458/0.9540	32.572/0.9597	33.041/0.9478

Specifically, for an input $F_{HV} \in \mathbb{R}^{U \times V \times C \times H \times W}$, we first reshape it into $X_S \in \mathbb{R}^{(UV) \times C \times H \times W}$. We employ depth-wise separable convolutions $W_{(\cdot)}$ to project X_S into query (Q), key (K), and value (V) embeddings:

$$Q = W_Q(X_S), \quad K = W_K(X_S), \quad V = W_V(X_S). \quad (10)$$

However, spatial attention derived solely from Q and K is limited to capturing intra-view texture similarities, often overlooking the geometric consistency inherent in light fields. To bridge this gap, we introduce a parallel angular prior branch. Specifically, we reshape the input F_{HV} into macropixels $X_A \in \mathbb{R}^{(HW) \times C \times U \times V}$ to explicitly model angular patterns, which are extracted via convolution f_{ang} and compressed by projection ϕ . Finally, we employ an additive broadcasting operation \mathcal{R} to generate the pairwise attention bias, defined as $B_{i,j} = \phi(x_i) + \phi(x_j)$ for spatial positions i and j . The formulation of the angular prior A_{prior} is given by:

$$A_{prior} = \mathcal{R}(\phi(f_{ang}(X_A))). \quad (11)$$

The angular prior A_{prior} is integrated into the spatial attention mechanism to impose geometric constraints. We

concatenate the spatial affinity $Q \cdot K^T$ with A_{prior} and apply a fusion layer \mathcal{F}_{mix} to generate the attention map:

$$Attn_{map} = \sigma(\mathcal{F}_{mix}([Q \cdot K^T, A_{prior}])), \quad (12)$$

$$F_i = Attn_{map} \odot V + F_{HV}, \quad (13)$$

where σ denotes the activation function and \odot represents element-wise multiplication. This modulation integrates texture similarity with angular consistency, thereby enhancing reconstruction in texture-less regions with depth structures.

III. EXPERIMENTS

A. Experimental Settings

Datasets and Preprocessing. We evaluate our method on five publicly available datasets: EPFL [23], INRIA [24], STFgantry [25], HCInew [26], and HCIold [27]. Experiments use the central 5×5 SAIs, with training patches extracted via a sliding window from high-resolution images and downsampled by a factor of 4 using bicubic interpolation. The proposed model is trained for 100 epochs on 4 NVIDIA GeForce RTX 3090 GPUs. We employ the Adam optimizer with $\beta_1 = 0.9$ and $\beta_2 = 0.999$, and use the L1 loss as our optimization objective. The initial learning rate is set to 2×10^{-4} and is decayed by

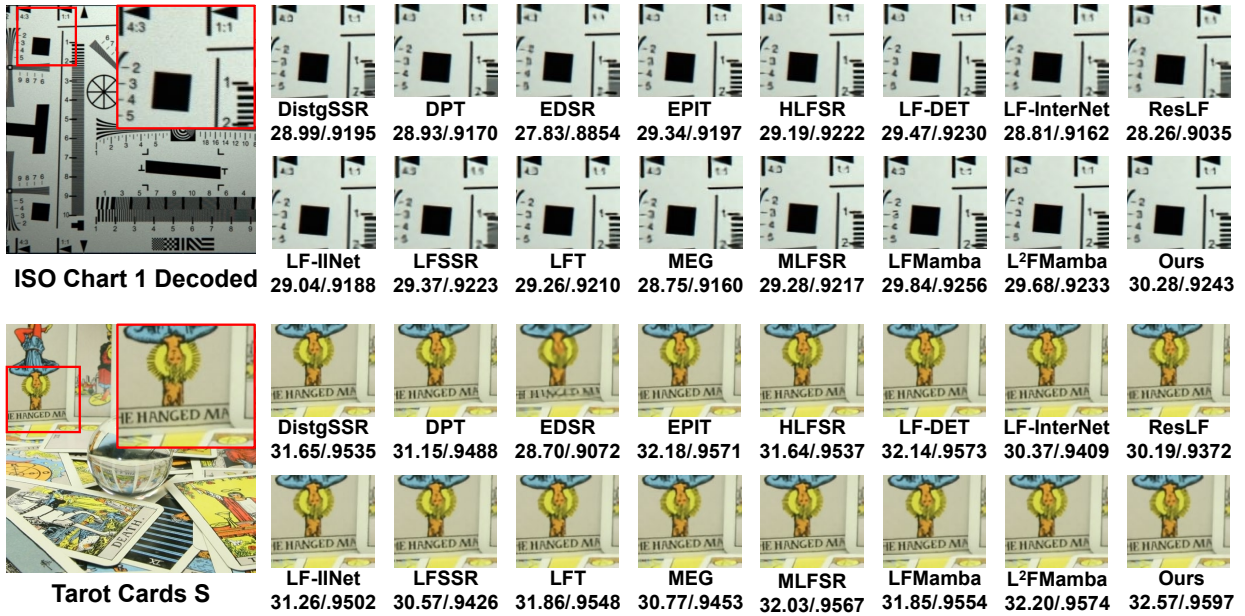


Fig. 3. Visual comparison of $4\times$ super-resolution results on real-world datasets. The first images show the full scene or cropped patches, while subsequent images display the zoomed-in details of the red box regions.

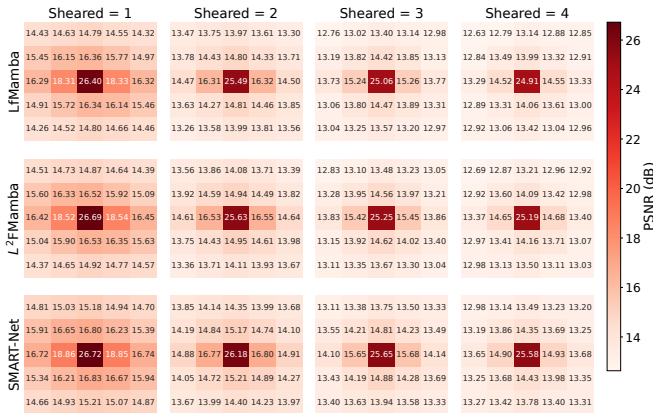


Fig. 4. PSNR distribution across different sheared EPIs on STFgantry.

50% every 25 epochs. The batch size is set to 2. For the disparity hypothesis set, we initialize $K = \{-2, -1, 0, 1, 2\}$.

B. Comparison with State-of-the-Art Methods

Quantitative Results. As summarized in Tab. I, SMART exhibits significant superiority over more than 20 representative LFSR methods, achieving an average PSNR of 33.040 dB and an SSIM of 0.9478. With a comparable parameter count, SMART achieves a PSNR gain of 0.417 dB over the previous state-of-the-art method, $L^2Fmamba$. This substantial performance gain validates the exceptional capability of SMART in modeling complex geometric consistency and reconstructing high-frequency texture details.

Qualitative Results. Fig. 3 illustrates the visual comparison of super-resolution reconstruction results on two real-world datasets. When dealing with fine structures such as text,

TABLE III
ABLATION STUDY ON THE NUMBER OF INTERACTION BLOCKS

Blocks	Params (M)	GFLOPs	Time (ms)	Avg. PSNR/SSIM
3	1.26	62.94	35.08	32.451/0.9428
4	1.61	82.33	56.65	32.663/0.9439
5	1.98	101.72	70.66	33.040/0.9478
6	2.34	121.12	86.27	32.775/0.9459

TABLE IV
QUANTITATIVE COMPARISON OF DIFFERENT SCANNING STRATEGIES FOR $4\times$ LIGHT FIELD SUPER-RESOLUTION.

Forward (F)	Backward (B)	slope-guided (SG)	EPFL PSNR / SSIM	INRIA PSNR / SSIM
✓	✓		29.584/0.9234	31.551/0.9544
✓		✓	29.949/0.9213	32.149/0.9521
	✓	✓	30.014/0.9219	32.251/0.9528
✓	✓	✓	30.284/0.9243	32.458/0.9540

typical methods, including those based on mamba, often suffer from blurred strokes or distortion artifacts. In contrast, the SMART, by accurately modeling EPI features, is able to restore text outlines, producing reconstruction details that are most consistent with the GT.

Robustness to Scene Geometry. Fig. 4 illustrates the performance consistency concerning scene geometry on the STFgantry dataset. It demonstrates the PSNR distribution across varying disparity levels. It can be observed that SMART maintains higher PSNR compared to other methods across disparity range. This confirms that slope-guided adaptive scanning effectively aggregates features along epipolar lines, mitigating performance loss in complex-depth regions.

C. Ablation Study

Component Effectiveness. As shown in Tab. II, the spatial feature extraction establishes a solid foundation for light field reconstruction, yielding significant PSNR improvements of 2.7–4.2 dB across datasets. The Angle Prior guidance brings further gains of 1.5–2.6 dB, verifying the critical role of angular information in distinguishing complex light field structures. Finally, integrating the slope-guided adaptive scanning strategy boosts the average PSNR by 0.5 dB. This confirms that this strategy strictly aggregates features along epipolar lines to preserve geometric continuity, achieving more precise reconstruction than generic long-range modeling.

Impact of Cascade Blocks. Tab. III shows that as N increases from 3 to 5, the average PSNR rises from 32.451 dB to 33.040 dB. Since performance saturates at $N = 6$, we select $N = 5$ to balance accuracy and efficiency.

Scanning Strategies. As shown in Tab. IV, the standard rigid scanning (F+B) yields limited performance. Replacing either fixed direction with the slope-guided boosts performance to 30.014/32.251 dB. The full strategy achieves optimal results, demonstrating that the slope-guided deformable scanning adaptively aligns with light field disparity structures, compensating for the limitations of traditional fixed scanning.

IV. CONCLUSION

In this paper, we propose SMART to address the challenge of maintaining high-dimensional geometric consistency in light field super-resolution. SMART incorporates angular priors and epipolar-guided scanning to strengthen spatial-angular correlation and consistent sequence modeling, enabling precise feature aggregation along the intrinsic 4D light field manifold. Experimental results demonstrate that SMART outperforms state-of-the-art methods in reconstruction accuracy, while exhibiting robust capabilities in restoring intricate textures and mitigating geometric inconsistencies.

REFERENCES

- [1] Shunzhou Wang, Tianfei Zhou, Yao Lu, and Huijun Di, “Detail-preserving transformer for light field image super-resolution,” in *Proceedings of the AAAI Conference on Artificial Intelligence*, 2022.
- [2] Zhengyu Liang, Yingqian Wang, Longguang Wang, Jungang Yang, Shilin Zhou, and Yulan Guo, “Learning non-local spatial-angular correlation for light field image super-resolution,” in *Proceedings of the IEEE/CVF International Conference on Computer Vision (ICCV)*, October 2023, pp. 12376–12386.
- [3] Ruixuan Cong, Yu Wang, Mingyuan Zhao, Da Yang, Rongshan Chen, and Hao Sheng, “Rethinking the upsampling process in light field super-resolution with spatial-epipolar implicit image function,” in *Proceedings of the IEEE/CVF International Conference on Computer Vision*, 2025.
- [4] Yingqian Wang, Longguang Wang, Gaochang Wu, Jungang Yang, Wei An, Jingyi Yu, and Yulan Guo, “Disentangling light fields for super-resolution and disparity estimation,” *IEEE Transactions on Pattern Analysis and Machine Intelligence*, 2022.
- [5] Zhengyu Liang, Yingqian Wang, Longguang Wang, Jungang Yang, and Shilin Zhou, “Light field image super-resolution with transformers,” *IEEE Signal Processing Letters*, 2022.
- [6] Yue Liu, Yunjie Tian, Yuzhong Zhao, Hongtian Yu, Lingxi Xie, Yaowei Wang, Qixiang Ye, and Yunfan Liu, “Vmamba: Visual state space model,” *arXiv preprint arXiv:2401.10166*, 2024.
- [7] Ruisheng Gao, Zeyu Xiao, and Zhiwei Xiong, “Mamba-based light field super-resolution with efficient subspace scanning,” in *Proceedings of the Asian Conference on Computer Vision*, December 2024, pp. 531–547.

- [8] Yao Lu, Shunzhou Wang, Ziqi Wang, Peiqi Xia, Tianfei Zhou, et al., “Lfmamba: Light field image super-resolution with state space model,” *arXiv preprint arXiv:2406.12463*, 2024.
- [9] Zeqiang Wei, Kai Jin, Zeyi Hou, Kuan Song, and Xiuzhuang Zhou, “L²fmamba: Lightweight light field image super-resolution with state space model,” *IEEE Transactions on Computational Imaging*, 2025.
- [10] D Vint, G Di Caterina, JJ Soraghan, RA Lamb, and D Humphreys, “Evaluation of performance of vdsr super resolution on real and synthetic images,” in *2019 Sensor Signal Processing for Defence Conference (SSPD)*. IEEE, 2019, pp. 1–5.
- [11] Bee Lim, Sanghyun Son, Heewon Kim, Seungjun Nah, and Kyoung Mu Lee, “Enhanced deep residual networks for single image super-resolution,” in *The IEEE Conference on Computer Vision and Pattern Recognition (CVPR) Workshops*, July 2017.
- [12] Yulun Zhang, Kunpeng Li, Kai Li, Lichen Wang, Bineng Zhong, and Yun Fu, “Image super-resolution using very deep residual channel attention networks,” in *ECCV*, 2018.
- [13] Shuo Zhang, Youfang Lin, and Hao Sheng, “Residual networks for light field image super-resolution,” in *Proceedings of the IEEE/CVF conference on computer vision and pattern recognition*, 2019, pp. 11046–11055.
- [14] Henry Wing Fung Yeung, Junhui Hou, Xiaoming Chen, Jie Chen, Zhibo Chen, and Yuk Ying Chung, “Light field spatial super-resolution using deep efficient spatial-angular separable convolution,” *IEEE Transactions on Image Processing*, vol. 28, no. 5, pp. 2319–2330, 2018.
- [15] Jing Jin, Junhui Hou, Jie Chen, and Sam Kwong, “Light field spatial super-resolution via deep combinatorial geometry embedding and structural consistency regularization,” in *Proceedings of the IEEE/CVF conference on computer vision and pattern recognition*, 2020, pp. 2260–2269.
- [16] Yingqian Wang, Longguang Wang, Jungang Yang, Wei An, Jingyi Yu, and Yulan Guo, “Spatial-angular interaction for light field image super-resolution,” in *European Conference on Computer Vision*. Springer, 2020, pp. 290–308.
- [17] Yingqian Wang, Jungang Yang, Longguang Wang, Xinyi Ying, Tianhao Wu, Wei An, and Yulan Guo, “Light field image super-resolution using deformable convolution,” *IEEE Transactions on Image Processing*, vol. 30, pp. 1057–1071, 2021.
- [18] Shuo Zhang, Song Chang, and Youfang Lin, “End-to-end light field spatial super-resolution network using multiple epipolar geometry,” *IEEE Transactions on Image Processing*, vol. 30, pp. 5956–5968, 2021.
- [19] Gaosheng Liu, Huanjing Yue, Jiamin Wu, and Jingyu Yang, “Intra-inter view interaction network for light field image super-resolution,” *IEEE Transactions on Multimedia*, 2021.
- [20] Zhen Cheng, Yutong Liu, and Zhiwei Xiong, “Spatial-angular versatile convolution for light field reconstruction,” *IEEE Transactions on Computational Imaging*, vol. 8, pp. 1131–1144, 2022.
- [21] V. V. Duong, T. H. Nguyen, J. Yim, and B. Jeon, “Light field image super-resolution network via joint spatial-angular and epipolar information,” *IEEE Trans. Computational Imaging*, 2023.
- [22] Ruixuan Cong, Hao Sheng, Da Yang, Zhenglong Cui, and Rongshan Chen, “Exploiting spatial and angular correlations with deep efficient transformers for light field image super-resolution,” *IEEE Transactions on Multimedia*, 2023.
- [23] Martin Rerabek and Touradj Ebrahimi, “New light field image dataset,” in *8th international conference on quality of multimedia experience*, 2016.
- [24] Xiaoran Jiang, Mikael Le Pendu, Reuben A Farrugia, and Christine Guillemot, “Light field compression with homography-based low-rank approximation,” *IEEE Journal of Selected Topics in Signal Processing*, vol. 11, no. 7, pp. 1132–1145, 2017.
- [25] Mikael Le Pendu, Xiaoran Jiang, and Christine Guillemot, “Light field inpainting propagation via low rank matrix completion,” *IEEE Transactions on Image Processing*, vol. 27, no. 4, pp. 1981–1993, 2018.
- [26] Katrin Honauer, Ole Johannsen, Daniel Kondermann, and Bastian Goldluecke, “A dataset and evaluation methodology for depth estimation on 4d light fields,” in *Asian conference on computer vision*. Springer, 2016, pp. 19–34.
- [27] Sven Wanner, Stephan Meister, and Bastian Goldluecke, “Datasets and benchmarks for densely sampled 4d light fields,” in *VMV*, 2013, vol. 13, pp. 225–226.